

## GSA DATA REPOSITORY 2014352

### Profile of a paleo-orogen: High topography across the present-day Basin and Range from 40 to 23 million years ago

Elizabeth J. Cassel<sup>1\*</sup>, Daniel O. Breecker<sup>2</sup>, Christopher D. Henry<sup>3</sup>, Toti E. Larson<sup>2</sup>, and Daniel F. Stockli<sup>2</sup>

<sup>1</sup>*Department of Geological Sciences, University of Idaho, Moscow, Idaho 83844, USA*

<sup>2</sup>*Department of Geological Sciences, University of Texas at Austin, Austin, Texas 78712, USA*

<sup>3</sup>*Nevada Bureau of Mines and Geology, University of Nevada, Reno, Nevada 89557, USA*

\*[ecassel@uidaho.edu](mailto:ecassel@uidaho.edu)

#### Sedimentary Sequence

Regional stratigraphic trends in deposition can be directly compared with paleoelevation trends recorded by  $\delta D$  values of volcanic glass. Paleogene strata show that the locus and style of deposition shifted from eastern Nevada in the Eocene to central Nevada in the Oligocene, coincident with a depositional hiatus in northeastern Nevada. Relative elevations, determined from these ignimbrite correlations and new sedimentologic data, demonstrate that the hinterland was elevated, supporting the conclusions of the stable isotope data. This resolves an ambiguity inherent in stable isotope paleoaltimetry: the similarity of stable isotope compositions of meteoric water in low elevation rain shadows and high elevation orogens (Horton et al., 2004). The sequence is characterized by two dominant depositional styles, distinct in grain sizes, sedimentary structures, bed geometry, and sorting. Figure DR1 shows the general stratigraphic sequence in each region across the paleotopographic transect (Fig. 1). These features provide the basis for interpretations of depositional environments and correlations to the ages and locations of the sediments.

Eocene strata in eastern Nevada, such as the Elko Formation, typically compose fluvial gravel conglomerate packages up to 200 m thick deposited on basement, overlain by a sequence of interbedded fine-grained lacustrine sediments that can exceed 1000 meters in thickness. Packages characterized by organized traction-structured deposition, cut and fill, moderate sorting, clast imbrication, interbedded sand lenses, thin fine-grained overbank muds and paleosols are products of fluvial deposition in gravel-bed braided rivers (Miall, 1996). Eocene samples 11036DC, 09022NV, 11019EU, 11020EU, 11022EU, and 11021EU were all collected from ignimbrites directly overlying or interbedded with fluvial deposits of this type. Clast imbrication, alignment, and planar tabular cross-bedding are present. Beds are laterally continuous with variable thickness for 8-12 m or are cut by scour fills. Interbedded planar and trough cross-bedded fine to very coarse sand with granules-pebbles are common, and fine sand-silt beds with paleosol development features also occur throughout the section. Overlying interbedded laminated marl, siltstone, tuff, and carbonaceous mudstone containing abundant fossil flora, gastropods, and ostracods indicate deep freshwater lacustrine deposition and increased accommodation. Further up section, alternating micro-laminated kerogen-rich marl and calcareous mudstone, mud-cracked siltstone, stromatolites, and an absence of bioturbation record

anoxic, saline bottom waters and fluctuating profundal to evaporative conditions (Carroll and Bohacs, 1999), reflecting ponding of continental drainages and basin closure in the middle to late Eocene. Interbedded ashes were sampled for isotope analysis (samples 12099ES, 12018TC, 12105EH, 12139SR, and 12175CB; see Table DR1), and all recorded highly evaporated and enriched  $\delta D$  values. Thick packages of lacustrine sediments evidence increased accommodation and ponding of continental drainages in the Eocene, which ceased by early Oligocene, beginning a period of regional non-deposition. It is unlikely that local geomorphic damming provided the regionally extensive driver necessary to pond multiple drainages.

In western and central Nevada, thin alluvial and fluvial conglomerates and interbedded sands range from 2-10 m in thickness (Fig. 1), and compose a mix of debris flow and traction current structures indicating deposition on stream-flow dominated alluvial fans or in gravel-bed braided systems (Miall, 1996). The base of the section composes gravel conglomerate deposited on basement and dominated by clasts reflecting local and regional source terranes, including the underlying Paleozoic rocks and the upper and lower plates of the Roberts Mountain Allochthon (Dickinson, 2006). Western and central Nevada glass samples were collected from ignimbrites interbedded with or directly overlying these fluvial deposits. Packages are up to 200 m thick and maximum clast sizes range from small cobbles to medium boulders. Individual beds compose sand-matrix-supported granule-cobble conglomerate or clast-supported pebble-cobble and granule-pebble conglomerate with a sand-mud matrix. Beds are poorly to moderately sorted and contain 50-95% sub-angular to rounded clasts to matrix, with occasional interbeds of well-sorted pebble-cobble conglomerate. Beds are typically cemented with iron oxides or calcite. Sharp grain size changes and variable matrix-to-clast ratios between beds are common. Very poorly sorted matrix-supported pebble-coarse sand conglomerate beds characterized by discontinuity or scour fill geometries and lack of sorting and traction structures indicate extremely rapid, high-energy debris flow deposition. Interbedded scour fills, channelized deposition, thin overbank muds, and rip-up clasts indicate fluvial erosion and transport on stream-flow dominated alluvial fans (Miall, 1996). Multiple cut and fill, scour, and channel features within a bed, moderate sorting, channel geometries, imbrication or clast alignment, cross-bedding, interbedded sands, and thin interbedded fine-grained overbank muds and paleosols become more common up section indicating the dominance of the braided fluvial depositional environment (Miall, 1996; Sambrook Smith et al., 2006). Coarse grain sizes are present throughout the conglomerate sections. Lenses, scour fills, and lateral accretion elements are present, and beds are commonly graded. Localized, high-energy deposits suggest a response to a change in slope. Alluvial fans, formed at significant slope changes, likely fed coarse sediment into braided streams. Westward-flowing rivers (Fig. 1) and correlative ignimbrites record relatively higher elevations in central-eastern Nevada than to the west from late Eocene to late Oligocene.

Locally in central Nevada, these conglomerate deposits are overlain by 5-20 m of freshwater lacustrine strata composing very thinly bedded (1-10 cm) fine sand, silt, mud, and micritic limestone. Central Nevada lacustrine deposits suggest shallow lakes with regular fluvial input, including floodplain and fluvial channel deposits (Carroll and Bohacs, 1999). Depositional characteristics are most closely associated with the open basin fluvial-lacustrine facies of Carroll and Bohacs (1999), although some locations record evolution into closed basins with evaporite deposition. Mixed fossiliferous carbonate-siliciclastic beds, soft-sediment deformation, periodic rippled beds, mud-cracks, and rip-up clasts suggest repeated shoreline progradation into a hydrologically open lake. Low organic matter content and intermittent cross-bedded, channelized

sands and paleosols indicate periodic fluvial and floodplain deposition and shoreline migration (Carroll and Bohacs, 1999). The locus of deposition shifted to central Nevada, indicated by accumulations of Oligocene fluvial, alluvial fan, and limited freshwater lacustrine sediments, as well as the formation of an erosional unconformity during that time in eastern Nevada.

## Methods

### *Hydrogen isotope compositions of hydration water in volcanic glass*

Silicate glasses record the hydrogen isotope compositions ( $\delta D$ ) of meteoric water shortly after deposition. Precipitation percolating through ignimbrite deposits replaces mobile cations in the glass, followed by the development of impermeable, high-density silicate gel layer near the glass surface (in  $<10$  ky) (Caillateau et al., 2008; Valle et al., 2010; Cassel et al., 2012). We tested the use of acid abrasion, as the surface outside of the silicate rind may still interact with ambient waters over geologic time-scales. Abrasion with Hydrofluoric acid twice for 25 seconds, followed by DI water rinsing, results in effective removal of the outermost glass surface. Samples that have not been acid abraded consistently show significantly higher  $\delta D$  values and less variability between samples from various geographic locations, likely reflecting the interaction of modern waters with the glass surface (outside of the gel layer). Glass sourced from ignimbrites are especially well-suited for paleoaltimetry, as hydrated glass rinds remain impermeable on geologic time-scales, faithfully recording the  $\delta D$  values of meteoric water, while ignimbrites and underlying sediments record relative elevations.

Bulk unwelded ignimbrite samples were taken from natural surface outcrops throughout the study area, and were selected at multiple locations along an outcrop from 10-30 cm under the surface exposure. All known northern Nevada Oligocene ignimbrite exposures were sampled to determine suitability for analysis. Volcanic glass fractions of 99% purity were prepared by crushing each sample in a ceramic mortar and then wet-separating into size fractions in using plastic sieves and nylon mesh screens with opening diameters of 150, 70, and 38  $\mu m$ . The 70-150  $\mu m$  mesh fraction was treated three times in 10% HCl for 60 seconds, then soaked and washed thoroughly in distilled water to remove any carbonate minerals. Samples were treated twice with 8% HF for 25 seconds to remove the surface rinds – outside the silicate gel layer (Cassel et al., 2012), washed repeatedly in distilled water, and dried. Repeated passes through a Frantz Isodynamic Separator removed magnetic minerals. Glass was gravity separated from quartz and feldspar in methyl iodide liquid. The purity, glass quality, and absence/presence of clays of each sample were checked thoroughly with a petrographic microscope prior to analysis. Only samples with no visible alteration minerals or dissolution were analyzed.

Hydrogen isotope ratios were measured in the Light Stable Isotope Lab at The University of Texas at Austin by high temperature thermal combustion and continuous-flow gas mass spectrometry using a Thermo Electron TC-EA coupled to a Thermo MAT253 isotope ratio mass spectrometer. 2-3 mg of 70-150  $\mu m$ , acid-abraded glass shards were enclosed in silver foil, dried under vacuum at 70°C, and then immediately flushed with dry He gas within a zero-blank auto sampler. Four internationally referenced standard materials and in-house working standards were run with the samples, and 3-8 repeat analyses were run on each glass separate to quantify the precision and accuracy of each analysis. The raw isotope data was then corrected for drift over time of the thermal combustion reactor and offset from the values of certified international

reference standards. Based on repeated analyses of IBS-22 (oil) and IBS-CH7 (foil) hydrogen standards, as well as comparisons of internal laboratory glass and kaolinite standards, precision for hydrogen isotope ratios was determined to be 2‰. All isotopic ratios are reported relative to SMOW. Fully propagated two sigma errors, including both standard and aliquot precision, are shown in Figure 2.

#### *Thermodynamic air-mass lifting Rayleigh condensation model (rainout model)*

Isotopic lapse rates used to calculate paleoelevations from measured  $\delta D$  values of ignimbrite glass were determined using an air-mass lifting and Rayleigh distillation model (Rowley et al., 2001). The model calculates the change in  $\delta D$  values of precipitation resulting from progressive condensation (and immediate removal from the air mass as precipitation) as a humid air mass rises and cools adiabatically. The model considers temperature dependent changes in the equilibrium isotope fractionation factor between vapor and liquid that occur as the air mass rises. The model also considers the temperature dependent vapor-ice fractionation factor for subfreezing temperatures (weighted averages of vapor-liquid and vapor-ice fractionation factors are calculated for temperatures between 273.15 and 253.15 K, (Rowley et al., 2001)). The weighted average isotopic composition of water condensing over a range of altitudes ( $1500 \pm 500$ m) above any given point on the ground surface is also considered (Rowley et al., 2001). Although only a single low elevation vapor source is considered, secular changes in the isotopic composition of the vapor source are accounted for when applying the model to the volcanic glass record by using low elevation datums. New U-Pb analyses in zircon from low elevation ignimbrites yielded eruption ages of  $30.1 \pm 1.5$  and  $23.6 \pm 1.9$  Ma. We use the  $\delta D_{\text{glass}}$  values of these ignimbrites as early and late Oligocene low elevation datums, respectively (Table DR1).

The geometrical controls on orographic precipitation (Roe and Baker, 2006) are not considered here. Air mass mixing and evaporation of hydrometeors, among other processes, are also not accounted for in the model used here, although they have been accounted for in some isotope-enabled climate models (Feng et al., 2013). Our consideration of air mass mixing is discussed in the main text. Evaporation of hydrometeors would result in less negative  $\delta D$  values of precipitation reaching the ground surface at any given elevation. If the magnitude of this effect is the same at all elevations, then it would have no influence on the  $\delta D$  lapse rate and thus no influence on the paleoelevations calculated here (it would, however, influence the  $\delta D$  value of initial vapor determined by fitting the model to modern surface water data, see below). An increase (decrease) in the magnitude of the evaporation effect with elevation would mean that the  $\delta D$  lapse rates used here are too high (too low) and therefore the calculated paleoelevations reported here are minimum (maximum) values. The validation of the model using modern surface waters (see below) suggests that the processes considered by the model are sufficient for the modern Sierra Nevada.

The model was validated for this region by comparison with  $\delta D$  values of modern surface, spring, well, and precipitation waters (Ingraham and Taylor, 1991; Kendall and Coplen, 2001; Friedman et al., 2002) collected across California (Fig. DR2). The land surface elevations corresponding to the precipitation sourcing these surface waters were estimated by calculating the mean of the sampling elevation and the highest elevation in the catchment. For model validation, we used a datum of 900 mbar (about 1000 m above sea level) because the relevant data for air masses delivering precipitation to the Sierras is available for this altitude. The initial

temperature of the model air mass was taken to be 7°C, which was the 1948-1988 mean air temperature at 900 mbar over Oakland during precipitation events in the Sierra Nevada (Pandey et al., 1999), and the Oligocene temperature anomalies were added to this value to simulate Oligocene precipitation. Maximum paleoelevations were calculated using a maximum temperature anomaly (i.e. difference from modern MAT) of +7°C for low elevation coastal air masses. Minimum paleoelevations were calculated assuming no difference between Oligocene and modern initial air mass temperatures and best estimates were calculated using an Oligocene temperature anomaly of +2.5°C. We estimated an initial relative humidity (IRH) of 100% based on modern atmospheric measurements (Pandey et al., 1999), which suggests supersaturation at our 900 mbar datum. The model is relatively insensitive to IRH; IRH = 80% results in calculated paleoelevations that are lower than reported here by <5%. The  $\delta D$  value of initial water vapor that results in the best fit of the model to the data is -123‰. Comparison of this value with measurements of  $\delta D$  values of water vapor over Oakland during Sierra precipitation events would further test the model used here but we could not find such measurements reported in the literature.

Atmospheric flow is more likely to deflect around a wide orogen and more likely to go up and over a thin orogen, causing upwind lifting (Galewsky, 2009). Modeling the isotopic composition of modern precipitation across the Sierra Nevada does not require upwind lifting to fit with modern data. Therefore, we interpret that upwind lifting was not significant across the much wider ancient Nevada orogen.

Paleoelevations were calculated assuming that air mass temperatures at 1000 m along the Late Oligocene coast were 2.5°C higher than modern (SST 2.5°C higher than modern during Late Oligocene) (Zachos et al., 2001; Lunt et al., 2007). Minimum and maximum paleoelevations were estimated assuming that initial air mass temperatures were no less than modern and not greater than 7°C higher than modern, respectively. Sensitivity analysis indicated that paleoelevation errors resulting from RH uncertainty and propagated analytical error ( $\delta D$  measurements) are much smaller than errors resulting from initial temperature uncertainty. An F-test for the equality of slopes was performed for each dataset using the analysis of covariance tool in Matlab (see main text). Figure DR3 is graph of these data and the calculated regression lines. As shown by Poulsen and Jeffery (2011), warming leads to a reduction in the surface to upper troposphere vapor  $\delta D$  gradient. The thermodynamic air mass lifting Rayleigh condensation model used here also predicts a smaller  $\delta D$  lapse rate with increasing initial air mass temperature. A smaller temperature lapse rate results in less rainout and in a smaller increase with altitude in  $\alpha_{l-v}$ , which together result in a smaller  $\delta D$  lapse rate. Thus, if temperature lapse rates were smaller in past warmer climates, paleoelevations estimated using modern lapse rates are minimum values (Poulsen and Jeffery, 2011). The estimated effect of this process on estimated paleoelevations is shown in Figure 2B.

Currently, the crust across northern Nevada is 28-34 km thick with a relatively flat Moho (Fig. 1; Gilbert, 2012). Restoring an estimate of average extension across the northern Basin and Range (McQuarrie and Wernicke, 2005; Colgan and Henry, 2009; Best et al., 2013) results in an average crustal thickness of 52 km, consistent with previous thickness estimates from core complex geology (e.g., Coney and Harms, 1984; MacCready et al., 1997; Miller et al., 1999; McGrew et al., 2000) and volcanic geochemistry (Cassel et al., 2009a; Best et al., 2013). This was compared to an estimate of isostatic equilibrium using the surface elevations calculated with the rainout model and average crust, lithosphere, and mantle densities (50-55 km). Mid-crustal

rocks flowed from the regions of highest elevation into lower elevation areas of larger-magnitude upper crustal extension. This has been recorded locally in the Ruby Mountains, where ductilely deformed mid-crustal rocks are exposed (MacCready et al., 1997). The data presented here show, however, that mid-crustal flow occurred later and over a much broader area than previous extensional models have predicted, due to coupling of the Sierra Nevada to the Colorado Plateau/Wyoming Craton by the Farallon slab. The magmatic heat flux following slab removal weakened the middle crust, allowing for gravitationally forced mid-crustal flow that was spatially decoupled from upper-crustal deformation (Beaumont et al., 2006). Decoupled upper-crustal brittle deformation and melt-weakened mid-crustal flow are likely important coeval mechanisms for lowering surface elevations and distributing overthickened crust.

#### *U-Pb ages on ignimbrites using LA-ICP-MS*

U-Pb geochronology was conducted at the laser ablation high-resolution inductively coupled plasma mass spectrometry (LA-HR-ICP-MS) laboratory at the University of Texas at Austin. Zircon grains were separated from ignimbrites samples following standard heavy mineral separation techniques and mounted on epoxy pucks using double-sided tape. A Photonmachine Analyte G.2 193nm ArF Excimer laser (30  $\mu\text{m}$  spot diameter) with a large-volume Helex cell was used to ablate material to  $\sim 16\ \mu\text{m}$  depths in individual zircon grains. Ablation rate and depth were calibrated using a Bruker Contour GT-1K 3D Optical Interferometer for improved down-hole fraction correction. The ablated dry aerosol was introduced into an Element2 HR-ICP-MS using ultra-high purity He carrier gas for  $^{238}\text{U}$ ,  $^{232}\text{Th}$  and  $^{206-208}\text{Pb}$  isotopic measurements (using ion-counting). Each analysis consists of a six pulse cleaning ablation, a background measurement (laser off), a thirty-second measurement with the laser firing, and a thirty-eight second cleaning cycle. Elemental and isotopic fractionation of Pb/U and Pb isotopes, respectively, was corrected by interspersed analysis of primary and secondary zircon standards with a known age (e.g., GJ1, Plesovice, Mud Tank). The common unknown to standard measurement ratio is generally 4:1 at the UT laboratory. Uncertainty resulting from calibration correction is generally 1-2% for both  $^{206}\text{Pb}/^{207}\text{Pb}$  and  $^{206}\text{Pb}/^{238}\text{U}$ . All ignimbrite ages reported here are based on the average of the youngest population of individual concordant  $^{206}\text{Pb}/^{238}\text{U}$  ages (Fig. DR4).

**Table DR1.** Stable isotope data is shown in Figures 2 and DR2.

<i>Sample</i>	<i>Latitude</i>	<i>Longitude</i>	<i>Average <math>\delta D</math> (‰) 3-9 analyses</i>	<i>2<math>\sigma</math> Propo gated Error</i>	<i>Distance along transect (km)</i>	<i>Reconstructed Distance along transect (km)</i>	<i>Age (Ma)</i>	<i>Normalized <math>\delta D</math> (‰)</i>
08122VS*	38.21	120.84	-95.1	4.7	3	3.0	23.6*	0.0
09054BIA*	38.90	117.79	-170.3	6.0	290	248.8	24	-75.2
09055BI*	38.91	117.80	-149.9	4.0	291	249.6	24	-54.8
09051RR*	39.05	118.63	-145.2	4.7	225.7	183.6	24.9	-50.1
09053RW*	39.05	118.37	-147.5	5.6	248	194.0	24.9	-52.4
11012HS*	39.44	116.75	-184.9	6.5	398	305.7	24.96*	-89.8
09015NVB*	40.65	116.31	-167.0	5.4	476.1	332.8	25	-71.9
07105 REA	39.79	119.67	-139.2	4.1	166	157.1	25.01	-44.1
09052RW*	39.04	118.37	-164.3	4.3	247	193.5	25.1	-69.2
09048YR*	38.95	119.02	-140.7	4.2	188	164.0	27.12	-45.6
09047YR*	38.95	119.02	-139.3	4.5	188.5	164.5	27.12	-44.2
09046YR*	38.95	119.02	-146.7	4.1	189	164.8	27.12	-51.6
07019RE	39.66	119.78	-151.1	4.3	149	145.8	28.68	-38.7
06289	39.91	120.00	-158.8	6.7	143	138.6	28.69	-46.4
11028TRCA*	39.78	116.76	-154.6	4.9	408.5	294.2	28.7	-21.9
11028TRCB*	39.78	116.76	-149.8	11.7	408.5	294.2	28.7	-6.8
11027TRCA*	39.78	116.76	-164.2	5.7	409	294.4	28.7	-20.5
11027TRCB*	39.78	116.76	-151.4	8.3	409	294.4	28.7	-23.2
11010WC*	39.30	116.57	-170.3	4.6	407.8	307.6	28.7	-22.9
06052	39.32	120.80	-134.3	5.3	55	55.0	28.70	-34.1
06053	39.32	120.80	-119.2	8.1	55	55.0	28.70	-28.3
06160	39.32	120.80	-132.9	5.0	55	55.0	28.70	-45.6
07039OM	39.33	120.72	-135.6	4.9	61	61.0	28.70	-36.7
07057OM	39.33	120.69	-135.3	5.2	64	64.0	28.70	-39.1
06283	39.63	120.44	-146.5	7.6	96	96.0	28.70	-42.2
07021RE	39.66	119.78	-140.7	4.2	149	145.8	28.70	-37.4
09029NV*	39.94	117.14	-158.0	5.0	382	280.1	28.70	-51.8
09017NV*	40.28	117.18	-149.1	4.2	388.9	281.0	28.70	-39.0
09010NV*	40.21	117.02	-151.5	4.1	402.6	288.1	28.70	-57.9
09012NV*	40.81	116.30	-162.3	5.7	482.4	337.4	28.70	-49.9
09011NV*	40.81	116.30	-152.8	4.8	470	337.6	28.70	-40.4
09013NV*	40.81	116.30	-154.1	4.3	471	338.5	28.70	-41.7
06172	39.29	120.38	-144.6	4.9	88	88.0	28.74	-32.2
11009WC*	39.30	116.57	-161.2	5.9	408.8	308.7	28.90*	-48.8
08123VS*	38.17	120.86	-112.4	7.2	4	4.0	30.1*	0.0
06114	39.22	120.88	-126.9	5.9	43	43.0	30.89	-14.5
07055OM	39.33	120.72	-130.8	4.0	62	62.0	30.90	-18.4
07014PO	39.77	120.51	-153.3	5.3	97	97.0	30.90	-40.9
06273	39.22	121.00	-122.2	5.3	33	33.0	30.91	-9.8
06073	39.27	121.01	-126.1	7.1	34	34.0	30.91	-13.7

06267	39.28	121.00	-123.6	7.0	35	35.0	30.91	-11.2
06272A	39.23	120.92	-125.4	4.9	41	41.0	30.91	-13.0
06115	39.21	120.88	-126.2	4.2	43	43.0	30.91	-13.8
06271	39.26	120.91	-123.9	4.8	43	43.0	30.91	-11.5
06275A	39.60	120.59	-140.5	7.2	83	83.0	30.91	-28.1
06275B	39.60	120.59	-142.8	6.4	83	83.0	30.91	-30.4
06276	39.60	120.59	-141.3	5.7	83	83.0	30.91	-28.9
06284	39.77	120.59	-149.9	6.4	89	89.0	30.91	-37.5
06285	39.77	120.59	-148.4	5.9	89	89.0	30.91	-36.0
06288	39.81	120.49	-152.2	6.4	100	100.0	30.91	-39.8
07022PO	39.80	120.12	-142.8	12.2	130	125.9	30.91	-30.4
07114RE	40.03	119.94	-147.3	4.8	153	147.1	30.91	-34.9
09057SH*	39.79	117.64	-155.0	4.5	335	264.9	30.91	-42.6
06219	39.50	120.56	-144.7	5.5	82	82.0	31.00	-32.3
11002CG*	39.22	116.86	-156.4	8.0	380	284.7	31.01	-44.0
11001CG*	39.22	116.86	-157.5	7.2	379	284.9	31.07*	-45.1
07115PO	39.97	120.54	-151.6	5.0	101	101.0	31.24	-39.2
11024TRC*	39.77	116.77	-162.6	5.8	408	293.6	31.27*	-50.2
07005LP	39.70	120.99	-129.5	9.7	54	54.0	33.00	-17.2
11036DC*	39.98	116.80	-163.7	7.1	413.1	291.2	33.86*	-51.3
09022NV*	40.37	117.25	-150.8	4.3	390	276.3	34.20	-38.4
11021EU*	39.48	115.94	-174.8	7.1	467	358.9	36.33*	-62.4
11020EU*	39.41	115.92	-173.3	7.4	466	361.0	36.53*	-60.9
11019EU*	39.45	115.94	-164.5	5.6	466	359.2	36.63*	-52.1
11022EU*	39.51	115.97	-165.2	7.9	462	356.3	36.92*	-52.8
12099ES*	40.58	115.99	-66.7	9.4	500	352.5	37	45.7
12139SR*	40.58	115.99	-72.4	5.6	500	352.7	37.91*	40.0
12018TC*	41.28	116.11	-59.7	5.3	513	364.5	38	52.7
12105EH*	40.82	115.72	-67.7	27.1	531	379.1	38	44.6
12175CB*	41.76	115.47	-90.6	8.1	582	415.1	40	21.8
12154NC*	41.02	114.54	-168.4	4.8	636	447.3	40	-56.0
11044CM*	41.13	115.64	-147.4	6.3	548	390.3	40.7	-35.1

Average  $\delta D$  calculated from 3-9 aliquots;  $2\sigma$  propagated error includes both individual sample and analytical error. All new analyses and ages are identified by \* (Sierra Nevada data from Cassel et al., 2009b). Additional  $^{40}\text{Ar}/^{39}\text{Ar}$  data from Cassel et al. (2009a) and Henry et al. (2012). All ages from single crystal  $^{40}\text{Ar}/^{39}\text{Ar}$  in sanidine and plagioclase, except U-Pb zircon ages of 08122VS and 08123VS (in italics).



**Table DR2.** Modern stable isotope data shown in Figures 2 and DR2.

<i>Data Source</i>	<i>Type of Water Source</i>	<i>Latitude</i>	<i>Longitude</i>	<i>Distance along transect (km)</i>	<i>Average <math>\delta D</math> (‰)</i>	<i>Normalized <math>\delta D</math> (‰)</i>
Ingraham & Taylor 1991	Domestic well	39.234	-121.409	0	-64.0	0.0
"	Domestic well	39.2343	-121.409	13.8	-59	5.0
"	Domestic well	39.247	-121.137	37	-69.0	-5.0
"	Spring	39.243	-121.106	40	-68.0	-4.0
"	Spring	39.320	-121.033	47	-71.0	-7.0
"	Spring	39.330	-120.844	64	-77.0	-13.0
"	Spring	39.314	-120.785	69	-74.0	-10.0
"	Spring	39.323	-120.731	74	-78.0	-14.0
"	Spring	39.579	-120.702	82	-89.0	-25.0
"	Spring	39.432	-120.237	118	-105.0	-41.0
"	Spring	39.491	-120.364	109	-94.0	-30.0
"	Spring	39.357	-120.337	108	-91.0	-27.0
"	Spring	39.503	-120.288	116	-103.0	-39.0
"	Spring	39.486	-120.018	138	-111.0	-47.0
Coplen and Kendall, 2000	Average Multi-annual Stream	40.601	-122.443	15	-85.7	-21.7
"	"	37.676	-121.264	0	-79.4	-15.4
"	"	40.418	-120.671	118	-99.6	-35.6
"	"	39.432	-120.237	119	-104.8	-40.8
"	"	37.732	-119.558	102	-95.3	-31.3
"	"	39.778	-119.336	203.2	-83.3	-19.3
"	"	39.292	-119.311	193.5	-102.4	-38.4
"	"	36.875	-119.141	55	-98.4	-34.4
"	"	39.153	-119.097	209	-105.8	-41.8
"	"	40.467	-118.306	307	-102.6	-38.6
"	"	37.054	-118.226	132	-114.6	-50.6
"	"	41.775	-117.804	402	-113.4	-49.4
"	"	38.888	-117.244	341	-116.6	-52.6
"	"	40.728	-116.008	509	-119.7	-55.7
"	"	39.201	-114.688	555	-117.6	-53.6
Friedman et al., 2002	Weighted Annual Precipitation	39.192	-119.735	136	-109.0	-45.0
"	"	NA	NA	110	-108.0	-44.0
"	"	NA	NA	180	-105.0	-41.0
"	"	40.122	-114.875	572	-112.0	-48.0
"	"	39.322	-117.122	356	-119.0	-55.0
"	"	40.823	-115.790	525	-115.0	-51.0
"	"	39.468	-117.195	360	-120.0	-56.0
"	"	40.897	-117.805	347	-112.0	-48.0

"	"	40.718	-114.030	665	-100.0	-36.0
"	"	39.300	-114.842	536	-106.0	-42.0
"	"	39.025	-114.642	553	-112.0	-48.0
"	"	41.972	-114.658	641	-113.0	-49.0
"	"	39.318	-114.238	593	-115.0	-51.0
"	"	39.158	-114.608	557	-115.0	-51.0

Samples collected from domestic well, spring, stream, and precipitation waters (Ingraham and Taylor, 1991; Kendall and Coplen, 2001; Friedman et al., 2002).

## FIGURE CAPTIONS

Figure DR1. General stratigraphy of Eocene-Oligocene sedimentary and volcanic rocks across study area, compiled from field stratigraphic data at multiple locations within each region. Depositional differences between eastern, central, and western Nevada described in text and supplementary text.

Figure DR2. Modern surface water  $\delta D$  values from the Sierra Nevada, Coast Ranges, Great Valley, and Cascades (Ingraham and Taylor, 1991; Kendall and Coplen, 2001; Friedman et al., 2002) plotted versus current elevation, compared to the calibrated thermodynamic air mass lifting Rayleigh condensation model's calculated lapse rate elevations. Surface waters are detrended from latitude and corrected for mean drainage basin hypsometry using ArcGIS.

Figure DR3. Modeled current elevations of all modern surface water  $\delta D$  values, compared to a current mean elevation swath profile across the study region. Surface waters are detrended from latitude and corrected for mean drainage basin hypsometry using ArcGIS.

Figure DR4. Statistical comparison of  $\Delta\delta D$  gradients east of 110 km. Modern values are calculated from stream, spring, well, and precipitation data (Ingraham and Taylor, 1991; Kendall and Coplen, 2001; Friedman et al., 2002). Region east of the modern Sierra crest defined as 110-550 km from the eastern edge of the Great Valley where late Eocene Ione Formation paleoshoreline deposits outcrop (Bartow, 1992; Creely and Force, 2007). Early Oligocene slope and Eocene-early Oligocene combined slopes are similar within error, so the F-tests for equality of slopes were carried out by combining Eocene and early Oligocene data. The Eocene-early Oligocene and late Oligocene  $\delta D_{\text{glass}}$  gradients from west to east across Nevada differ from each other significantly ( $F = 9.26$ ,  $p < 0.01$ ), and both differ significantly from the modern gradient ( $F = 10.01$ ,  $p < 0.01$  and  $F = 18.03$ ,  $p < 0.01$ )

Figure DR5. Wetherill Concordia plots of individual concordant  $^{206}\text{Pb}/^{238}\text{U}$  ages from individual zircon grains used to calculate ignimbrite ages for samples 08122VS (A) and 08123VS (B). These analyses yielded eruption ages of A)  $23.6 \pm 1.9$  Ma and B)  $30.1 \pm 1.5$  Ma.

## REFERENCES CITED

- Bartow, J. A., 1992, Contact relations of the Ione and Valley Springs Formations in the east-central Great Valley, California.
- Beaumont, C., Nguyen, M. H., Jamieson, R. A., and Ellis, S., 2006, Crustal flow modes in large hot orogens, *in* Law, R. D., Searle, M. P., and Godin, L., eds., *Channel Flow, Ductile Extrusion and Exhumation in Continental Collision Zones*, Volume 268: London, Geological Society, Special Publications, p. 91-145.
- Best, M. G., Gromme, S., Deino, A. L., Christiansen, E. H., Hart, G. L., and Tingey, D. G., 2013, The 36–18 Ma Central Nevada ignimbrite field and calderas, Great Basin, USA: Multicyclic super-eruptions: *Geosphere*, v. 9, no. 5.
- Cailleteau, C., Angeli, F., Devreux, F., Gin, S., Jestin, J., Jollivet, P., and Spalla, O., 2008, Insight into silicate-glass corrosion mechanisms: *Nature Materials*, v. 7, p. 978-983.
- Carroll, A. R., and Bohacs, K. M., 1999, Stratigraphic classification of ancient lakes: Balancing tectonic and climatic controls: *Geology*, v. 27, p. 99-102.
- Cassel, E. J., Calvert, A. T., and Graham, S. A., 2009a, Age, geochemical composition, and distribution of Oligocene ignimbrites in the northern Sierra Nevada, California: implications for landscape morphology, elevation, and drainage divide geography of the Nevadaplano: *International Geology Review*, v. 51, no. 7, p. 723-742.
- Cassel, E. J., Graham, S. A., Chamberlain, C. P., and Henry, C. D., 2012, Early Cenozoic topography, morphology, and tectonics of the northern Sierra Nevada and western Basin and Range: *Geosphere*, v. 8, no. 2, p. 229-249.
- Cassel, E. J., Graham, S. A., and Chamberlain, P. C., 2009b, Cenozoic tectonic and topographic evolution of the northern Sierra Nevada, California, through stable isotope paleoaltimetry in volcanic glass: *Geology*, v. 37, no. 6, p. 547-550.
- Colgan, J. P., and Henry, C. D., 2009, Rapid middle Miocene collapse of the Mesozoic orogenic plateau in north-central Nevada: *International Geology Review*, v. 51, no. 9-11, p. 920-961.
- Coney, P. J., and Harms, T. A., 1984, Cordilleran metamorphic core complexes; Cenozoic extensional relics of Mesozoic compression: *Geology*, v. 12, no. 550-554.
- Creely, S., and Force, E. R., 2007, Type Region of the Ione Formation (Eocene), Central California: Stratigraphy, Paleogeography, and Relation to Auriferous Gravels: U.S. Geological Survey Open-File Report, v. 2006-1378, p. 65 p.
- Dickinson, W. R., 2006, Geotectonic evolution of the Great Basin: *Geosphere*, v. 2, no. 7, p. 353-368.
- Feng, R., Poulsen, C. J., Werner, M., Chamberlain, P. C., Mix, H. T., and Mulch, A., 2013, Early Cenozoic evolution of topography, climate, and stable isotopes in precipitation in the North American Cordillera: *American Journal of Science*, v. 313, p. 613-648.
- Friedman, I., Smith, G. I., Johnson, C. A., and Moscati, R. J., 2002, Stable isotope compositions of waters in the Great Basin, United States 2. Modern precipitation: *Journal of Geophysical Research*, v. 107, no. D19 (15), p. 1-22.
- Galewsky, J., 2009, Orographic precipitation isotopic ratios in stratified atmospheric flows: Implications for paleoelevation studies: *Geology*, v. 37, no. 9, p. 791-794.
- Gilbert, H., 2012, Crustal structure and signatures of recent tectonism as influenced by ancient terranes in the western United States: *Geosphere*, v. 8, p. 141-157.
- Henry, C. D., Hinz, N. H., Faulds, J. E., Colgan, J. P., John, D. A., Brooks, E. R., Cassel, E. J., Garside, L. J., Davis, D. A., and Castor, S. B., 2012, Eocene-Early Miocene paleotopography of the Sierra Nevada-Great Basin-Nevadaplano based on widespread ash-flow tuffs and paleovalleys: *Geosphere*, v. 8, p. 1-27.
- Horton, T. W., Sjostrom, D. J., Abruzzese, M. J., Poage, M. A., Waldbauer, J. R., Hren, M., Wooden, J., and Chamberlain, C. P., 2004, Spatial and temporal variation of Cenozoic surface elevation in the Great Basin and Sierra Nevada: *American Journal of Science*, v. 304, p. 862-888.

- Ingraham, N. L., and Taylor, B. E., 1991, Light stable isotope systematics of large-scale hydrologic regimes in California and Nevada: *Water Resources Research*, v. 27, p. 77-90.
- Kendall, C., and Coplen, T. B., 2001, Distribution of oxygen-18 and deuterium in river waters across the United States: *Hydrologic Processes*, v. 15, p. 1363-1393.
- Lunt, D. J., Ross, I., Hopley, P. J., and Valdes, P. J., 2007, Modelling late Oligocene C4 grasses and climate: *Palaeogeography, Palaeoclimatology, Palaeoecology*, v. 251, no. 2, p. 239-253.
- MacCready, T., Snoke, A. W., Wright, J. E., and Howard, K. A., 1997, Mid-crustal flow during Tertiary extension in the Ruby Mountains core complex, Nevada: *Geological Society of America Bulletin*, v. 109, no. 12, p. 1576-1594.
- McGrew, A. J., Peters, M. T., and Wright, J. E., 2000, Thermobarometric constraints on the tectonothermal evolution of the East Humboldt Range metamorphic core complex, Nevada: *Geological Society of America Bulletin*, v. 112, p. 45-60.
- McQuarrie, N., and Wernicke, B. P., 2005, An animated tectonic reconstruction of southwestern North America since 36 Ma: *Geosphere*, v. 1, p. 147-172.
- Miall, A. D., 1996, *The Geology of Fluvial Deposits*, Berlin Heidelberg, Springer-Verlag.
- Miller, E. L., Dumitru, T. A., Brown, R. W., and Gans, P. B., 1999, Rapid Miocene slip on the Snake Range-Deep Creek Range fault system, east-central Nevada: *Geological Society of America Bulletin*, v. 111, p. 886-905.
- Pandey, G. R., Cayan, D. R., and Georgakakos, K. P., 1999, Precipitation structure in the Sierra Nevada of California during winter: *Journal of Geophysical Research*, v. 104, no. D10, p. 12019-12030.
- Poulsen, C. J., and Jeffery, M. L., 2011, Climate change imprinting on stable isotopic compositions of high-elevation meteoric water cloaks past surface elevations of major orogens: *Geology*, v. 39, no. 6, p. 595-598.
- Roe, G. H., and Baker, M. B., 2006, Microphysical and geometrical controls on the pattern of orographic precipitation: *Journal of the Atmospheric Sciences*, v. 63, p. 861-880.
- Rowley, D. B., Pierrehumbert, R. T., and Currie, B. S., 2001, A new approach to stable isotope-based paleoaltimetry; implications for paleoaltimetry and paleohypsometry of the High Himalaya since the late Miocene: *Earth and Planetary Science Letters*, v. 188, no. 1-2, p. 253-268.
- Sambrook Smith, G. H., Ashworth, P. J., Best, J. L., Woodward, J., and Simpson, C. J., 2006, The sedimentology and alluvial architecture of the sandy braided South Saskatchewan River, Canada: *Sedimentology*, v. 53, no. 2, p. 413-434.
- Valle, N., Verney-Carron, A., Sterpenich, J., Libourel, G., Deloule, E., and Jollivet, P., 2010, Elemental and isotopic ( $^{29}\text{Si}$  and  $^{18}\text{O}$ ) tracing of glass alteration mechanisms: *Geochimica et Cosmochimica Acta*, v. 74, no. 12, p. 3412-3431.
- Zachos, J., Pagani, M., Sloan, L., Thomas, E., and Billups, K., 2001, Trends, rhythms, and aberrations in global climate 65 Ma to present: *Science*, v. 292, p. 685-693.

Figure DR1. General stratigraphy of Nevada sections.

Eastern Nevada

Northern  
Sierra  
Nevada

Central Nevada

Western Nevada

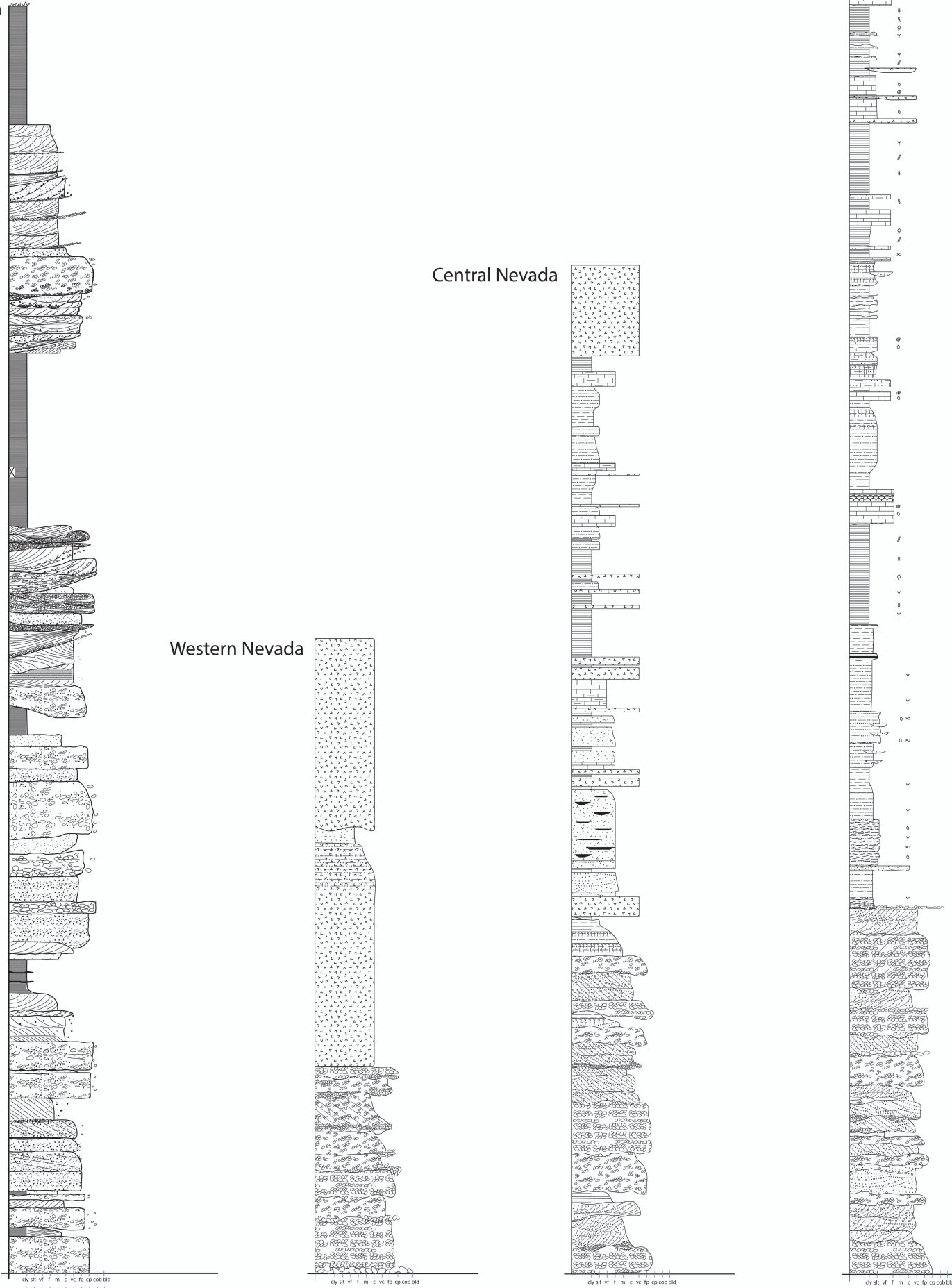
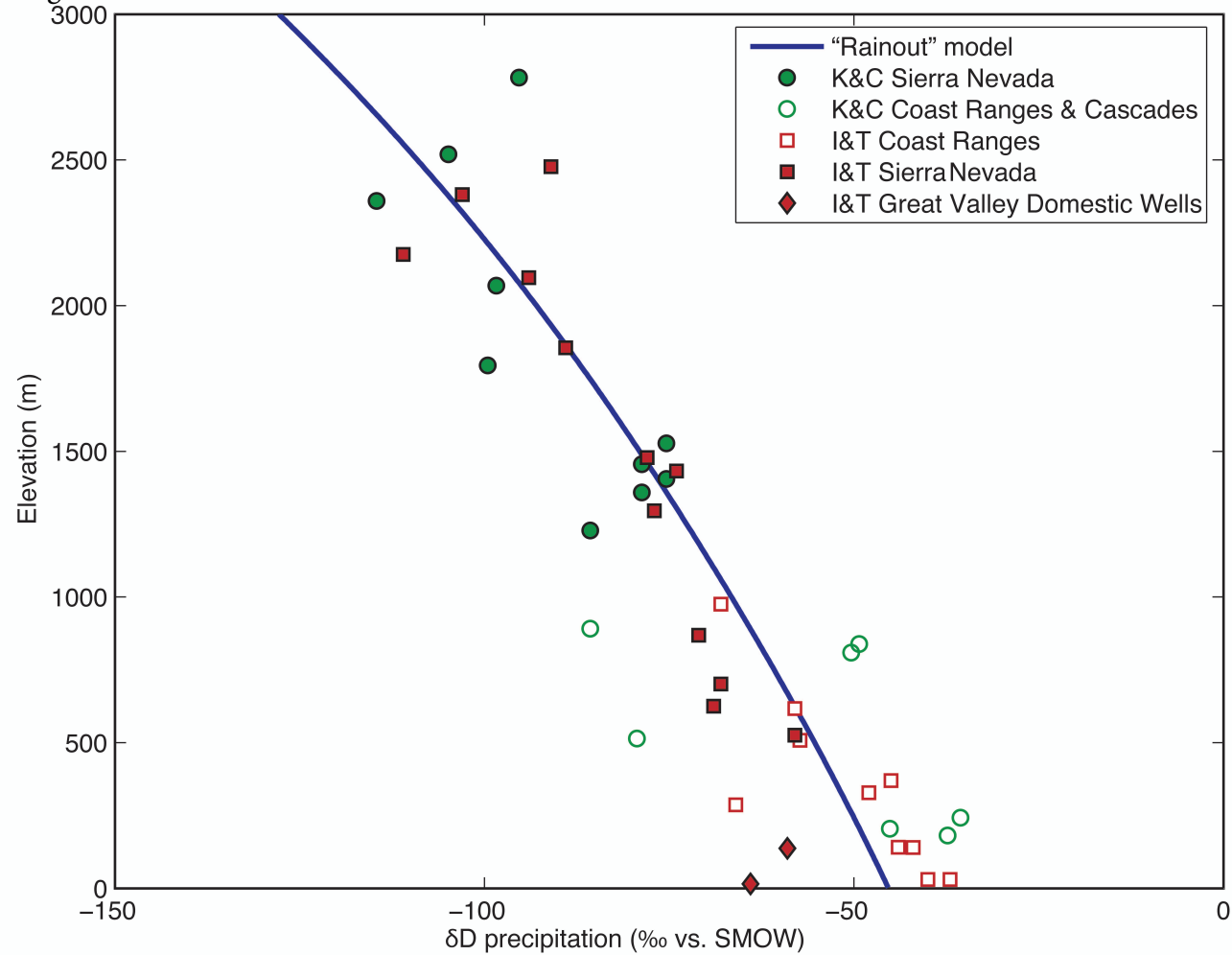


Figure DR2

## Model Calibration: Modern Data



# Modeled Elevations of Modern Data

Figure DR3

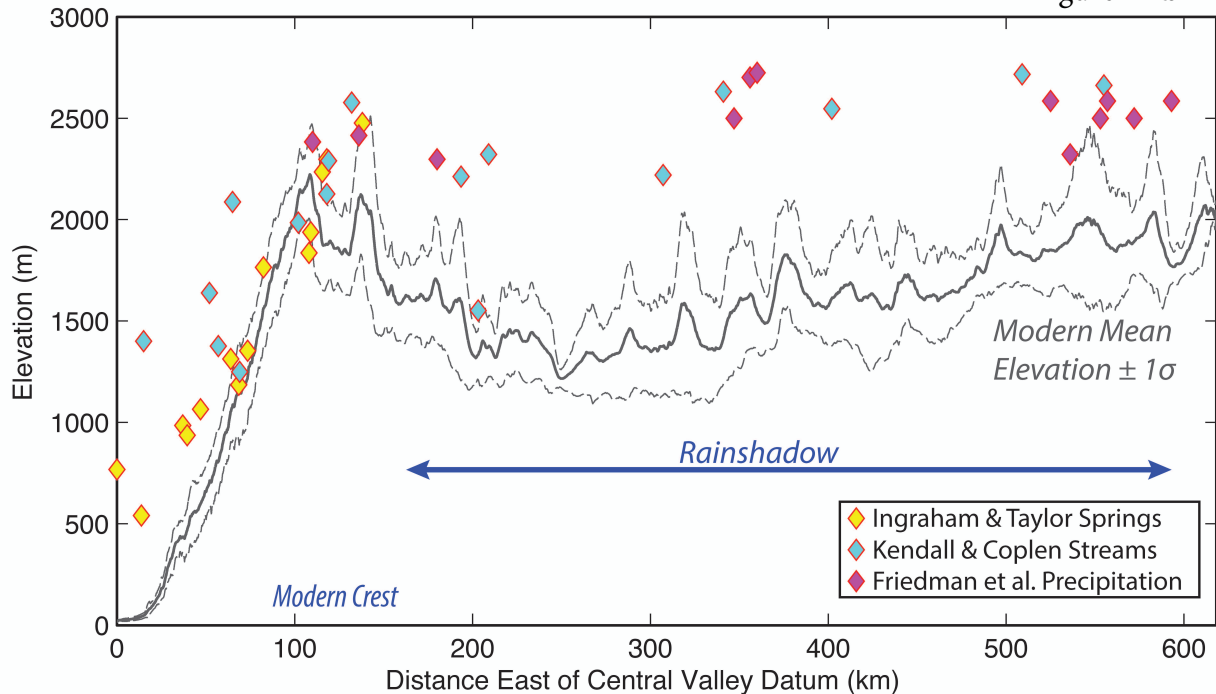
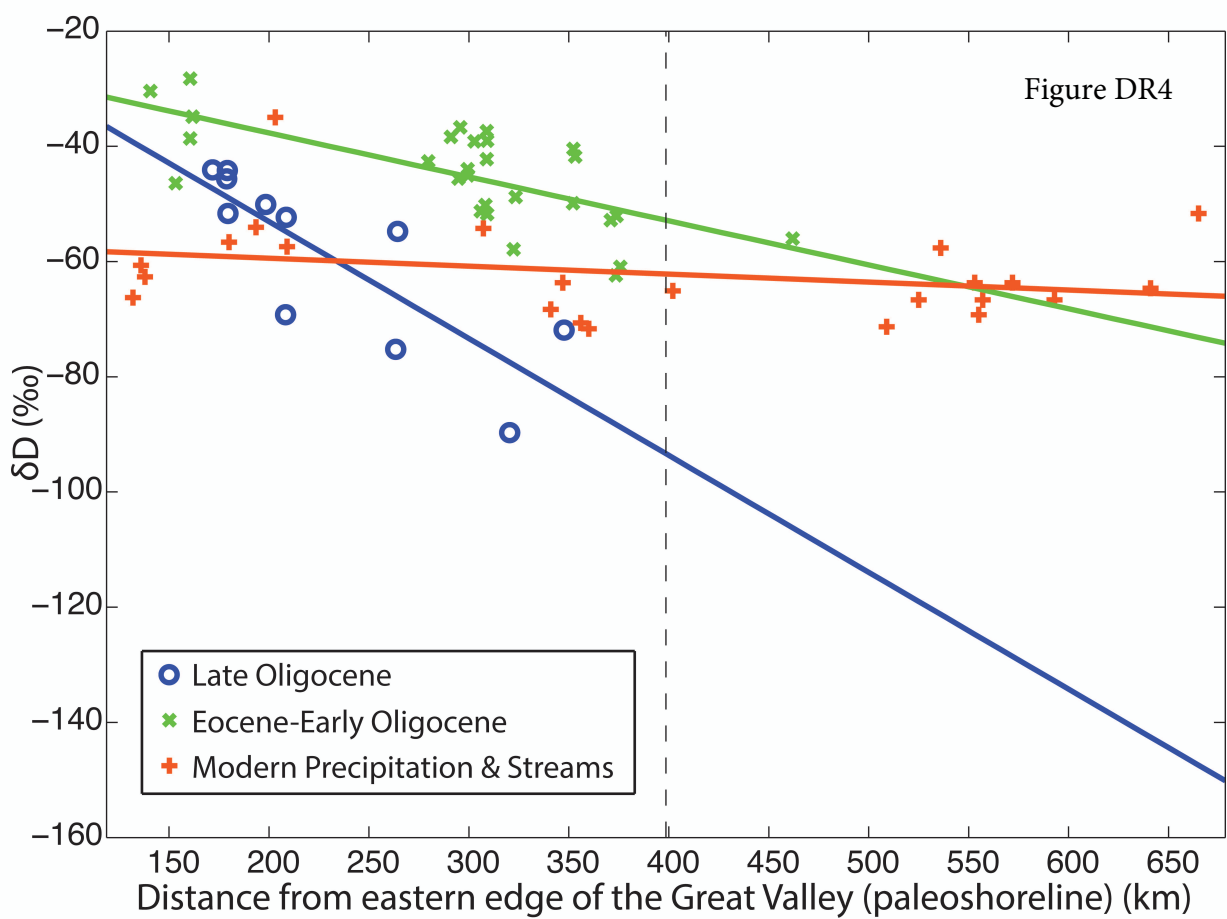


Figure DR4





A) 08122VS

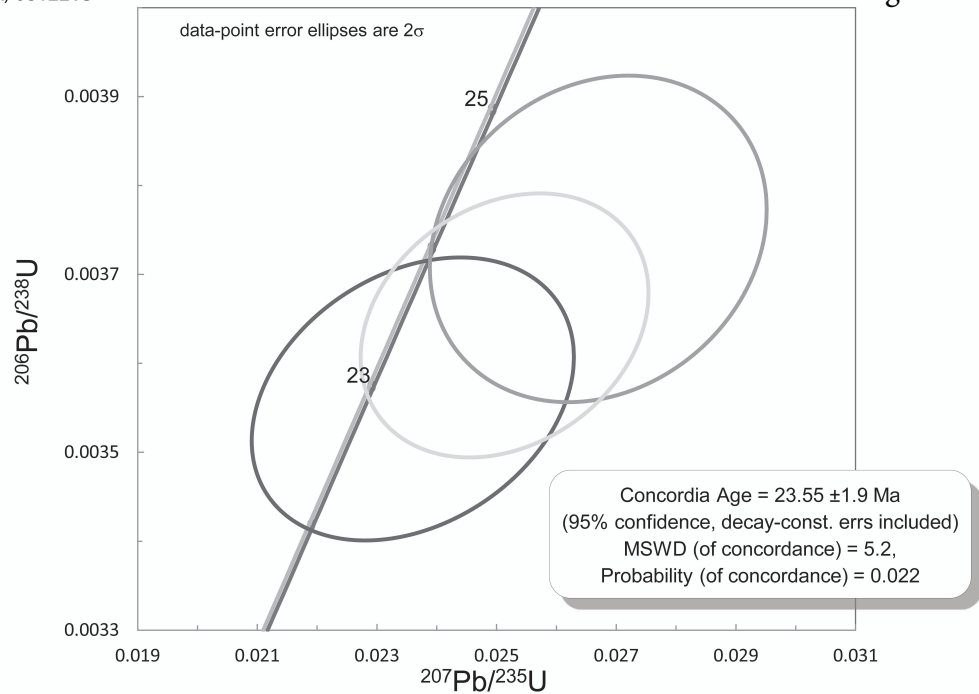


Figure DR5

B) 08123VS

